Supplemental Information for

Complex refractive indices in the ultraviolet and visible spectral region for highly absorbing non-spherical biomass burning aerosol

Caroline C. Womack[1,2], Katherine M. Manfred[1,2*], Nicholas L. Wagner[1,2], Gabriela Adler[1,2+], Alessandro Franchin[1,2§], Kara D. Lamb[1,2†], Ann M. Middlebrook[2], Joshua P. Schwarz[2], Charles A. Brock[2], Steven S. Brown[2,3], Rebecca A. Washenfelder[2]

[1]Cooperative Institute for Research in Environmental Sciences, University of Colorado, Boulder, CO 80309, USA
[2]Chemical Sciences Laboratory, National Oceanic and Atmospheric Administration, Boulder, CO 80305, USA
[3]Department of Chemistry, University of Colorado, Boulder, CO 80309, USA
*Now at Wolfson Atmospheric Chemistry Laboratories, Department of Chemistry, University of York, York, UK
+Now at Breezometer, Haifa, Israel
§Now at the National Center for Atmospheric Research, Boulder, CO 80305, USA
†Now at Department of Earth and Environmental Engineering, Columbia University, New York, NY 10027, USA

Correspondence to: Caroline C. Womack (caroline.womack@noaa.gov)

S1. Explicit accounting for drifts in stability in the new broadband cavity

Controlling the optical intensity and wavelength stability of the light source, spectrometer, and optics is critical in DOAS and BBCES measurements. The calculation of optical extinction requires the ratio of an analyte spectrum to the most recent reference spectrum or an interpolation between two recent reference spectra, and any drifts in the intensity of the light source or the mechanical positioning of the optical components will appear as a baseline offset or spectral shift in the optical extinction. When the light source and the cavity optics have broad, unstructured features as a function of wavelength, the drifts in the baseline are smoothly varying, and can be easily distinguished from highly structured extinction features. Fitting algorithms such as DOASIS (Kraus, 2006) and QDOAS (Danckaert et al., 2013) allow the user to include a polynomial in the fit to the data, without needing to know which type of optical stability is responsible for the drift.

The 400 – 720 nm cavity mirrors, however, do not have smoothly varying optical properties over the entire spectral region. Therefore, a simple polynomial is insufficient to account for instrument drift over time. Instead, we must explicitly account for each type of drift. The significant sources of drift are: 1) light source output intensity; 2) dark electrical current in the spectrometer; and 3) shifts in the spectrometer optics which lead to a drift in the pixel-to-wavelength calibration. Following the derivation of the expression for total light extinction in Appendix A of Washenfelder et al. (2008), we define the light intensity of a reference spectrum as

$$I_0(\lambda) = \frac{k_S I_{source}(\lambda)}{\frac{1-R(\lambda)}{d} + \alpha_{Rayleigh,0}(\lambda)} \tag{S1}$$

and the light intensity of the analyte spectrum as

$$I_{spec}(\lambda) = \frac{k_S I_{source}(\lambda)}{\frac{1-R(\lambda)}{d} + \alpha_{Rayleigh,spec}(\lambda) + \sum \alpha_i(\lambda)} \tag{S2}$$

The light extinction due to gas or aerosol absorbers or scatterers is defined as

$$\sum \alpha_i(\lambda) = \left(\frac{1-R(\lambda)}{d} + \alpha_{Rayleigh}(\lambda)\right)\left(\frac{I_0(\lambda)}{I(\lambda)} - 1\right) + \alpha_{Rayleigh,0}(\lambda) - \alpha_{Rayleigh,spec}(\lambda) \tag{S3}$$

To demonstrate the effect of each type of drift, we consider a spectrum, I_{spec}, with no absorbers (so $\Sigma\alpha_i$ in the denominator of Eq. S2 is set to 0) that has been affected by the three types of drift:

$$I_{spec}(C + \lambda) = \frac{A k_S I_{source}(\lambda)}{\frac{1-R(\lambda)}{d} + \alpha_{Rayleigh.spec}} + B \tag{S4}$$

A, B, and C are scalar factors that represent intensity changes of the light source, dark background, and spectrometer optics, respectively. Figure S1a shows an example of an extinction spectrum where A, B, and C are set to physically reasonable values of 0.999, 100 counts, and 0.002 nm, respectively.

It is clear from Fig. S2a that these drifts are responsible for the observed peaks in the measured spectra, such as the zero air spectrum shown in blue in Fig. S2b. Therefore, the peaks can be attributed to optical drifts, not real extinction by gas or aerosol species. Note that in the UV channel (360 – 385 nm), the drift observed still takes the form of a 4th-order polynomial, as those narrower band optical mirrors have smoothly varying reflectivity. To correct for the drifts in the visible channel (400 – 720 nm), we use a nonlinear Levenberg-Marquardt algorithm to find the set of parameters A, B, and C, which best replicate the observed spectrum. The result of that fit is shown in the red trace, and the black trace shows the corrected spectrum once that fit has been subtracted. Note that because Eq. S3 also depends on the mirror reflectivity, which is determined from measured spectra of He and CO_2 and can also experience drifts, a correction must also be made to the reflectivity measurement. While drifts in the reflectivity measurement are minor compared to the background spectrum, we include the parameters D, E, and F, analogously to Eq. S4. Therefore, there are six parameters in the total fit. This process is repeated for each averaged spectrum in this paper.

For spectra of ambient aerosol, or gas-phase NO_2, we can include these absorbers in the fit as well. In that case, the denominator of Eq. S4 has additional absorbers, described either by the literature absorption cross section of NO_2 (Vandaele, 1998) or a broadly changing polynomial for the ambient aerosol. This correction was made to all visible channel extinction spectra in the manuscript. Because it is difficult to differentiate between broadly changing aerosol extinction and broadly changing optical drifts in the UV channel, we use the fitted parameters from the visible channel to calculate and subtract the optical drift in the UV channel prior to the RI retrieval.

S2. Removal of spurious peaks in the SMPS size distribution at high diameters

For these measurements, an additional step was required to accurately process the SMPS scans. The inversion algorithm is designed to find the size distribution that, when inverted by the DMA transfer function, best replicates the particle concentration measured by the CPC during the SMPS scan. However, at the high voltage region of the SMPS scan, the number of particles is low and typically close to or below the detection limit of the

CPC. Therefore, the inverted size distribution often displays spurious values at large diameters (i.e. > 750 nm) that are non-physical representations of the aerosol size distribution produced by the atomizer. However, as shown in Fig. S4, a size distribution that has had these spurious values removed above a certain threshold, will result in a theoretical particle concentration trace that is still very close to that measured by the CPC. Often, these artifacts from SMPS scans are unimportant, as they represent only a very small percent of the total number of particles. However, large particles contribute disproportionately to the light extinction. Therefore, minor inaccurate counting of large particles can lead to very inaccurate retrievals of RI. As shown in Fig. S4c, ignoring CPC counts for SMPS voltage settings for particles >750 nm yields a set of size distributions that matches well with the OPC-derived size distributions, and we use this set of truncated size distributions to retrieve the RI.

Figure S1. The measured mirror reflectivity, total loss, and effective path length are shown in panel (a) for both the UV 360 – 385 nm mirrors and the very broadband visible 400 – 720 nm mirrors. The UV mirror optical properties are broad and unstructured, while the visible mirrors have rapidly changing reflectivity as a function of wavelength. Panel (b) shows the calculated and experimental lower detection limit in the 400 – 720 nm region for two minutes of averaging, as a function of wavelength. The black dashed line shows the theoretical limit, if the only source of error was detector shot noise. The red shows the observed lower detection limit when several hours of spectra were averaged when the cavity was filled with zero air. The lower detection limit assuming only shot noise is an order of magnitude lower, and is therefore negligible. Most of the error comes from instability in the light source and optics.
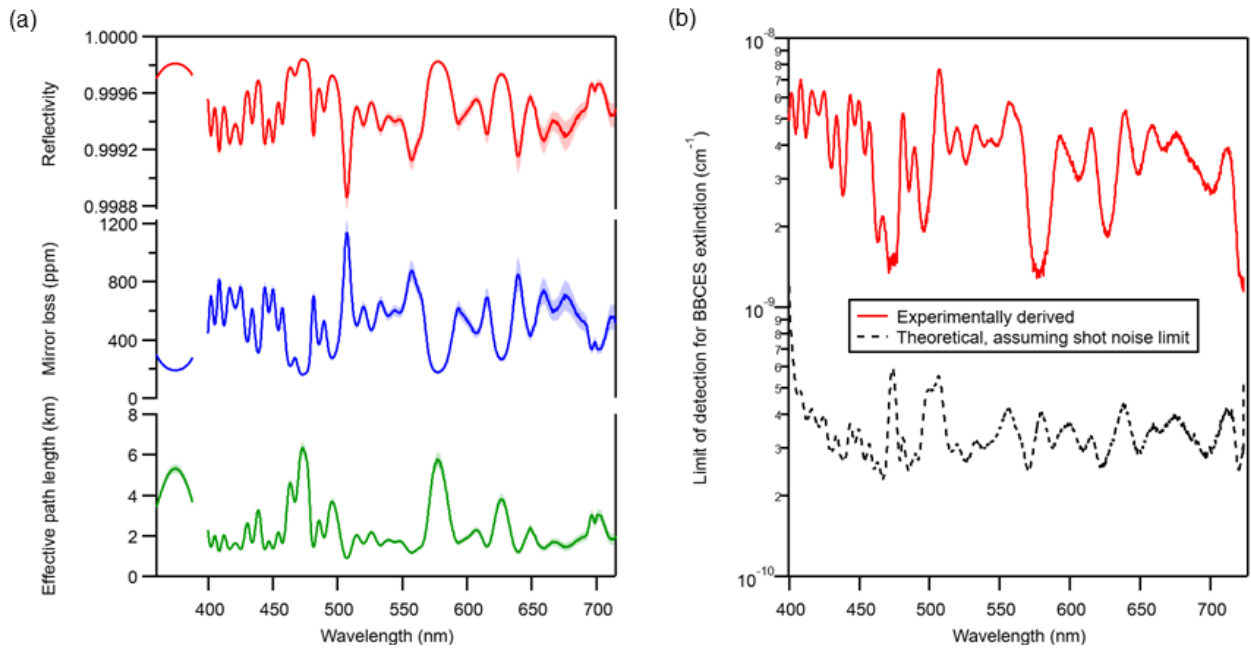
Figure S2. (a) Calculated change in the extinction spectra, assuming scalar changes in three components of the optical system: A = light source, B = dark background, C = spectrometer optics. (b) A sample spectrum of zero air, which should result in no absorption. However, the blue trace shows the measured spectrum, which displays the characteristic 4th-order polynomial for the narrower UV mirrors, and highly structured peaks that cannot be fit by a 4th-order polynomial for the broadband visible mirrors. The red trace shows the result of the multi-parameter fit designed to mimic the spectrum expected from the drift sources shown in panel a. The black trace shows the spectrum that has had this mirror-incurred structure removed, and the green trace shows the residual of the fit.
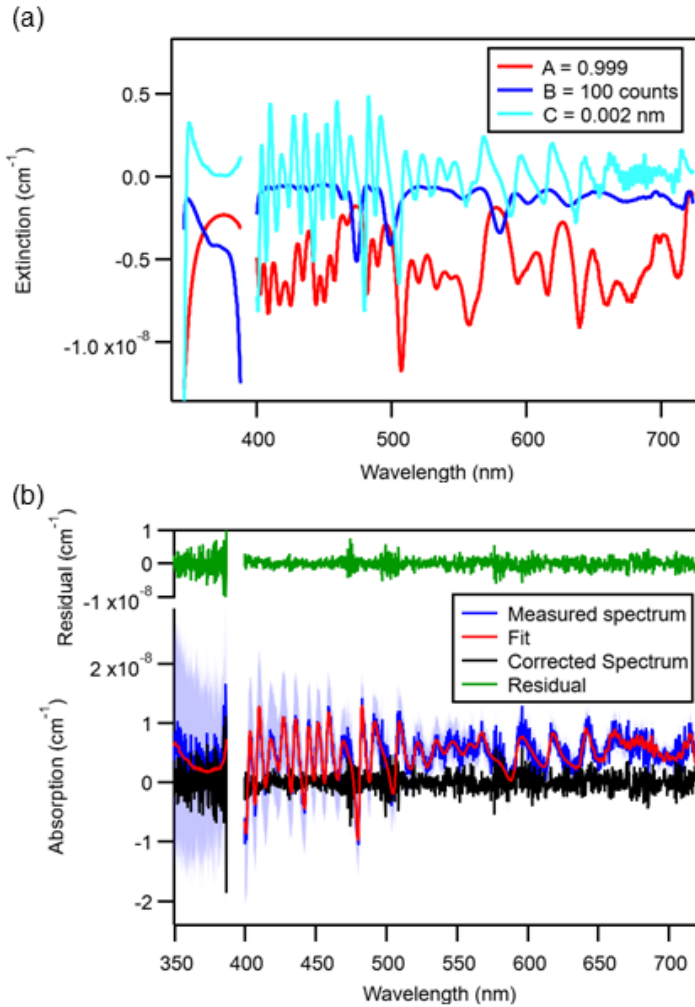
Figure S3. NO$_2$ measured during the FIREX 2016 study. Panels (a) and (b) show the retrieved NO$_2$ plotted against the nominal NO$_2$ calculated from the calibration tank concentration for the two BBCES channels. The colors vary from red (beginning of campaign) to purple (end of the campaign). In panel (c), the slope and r^2 of the linear fit to the retrieved and nominal NO$_2$ is shown for each campaign day, showing a slight drift downward in the slope, which may be attributed to change in the BBCES instrument or the NO$_2$ calibration tank. Panel (d) shows an example fit for 31 Oct 2016. The four NO$_2$ spectra are shown in colors, with the fitted spectrum shown in black. The average of the retrieved NO$_2$ for both channels is shown in the legend, and is quite close to the nominal concentrations (0, 24, 47, and 72 ppbv, respectively).
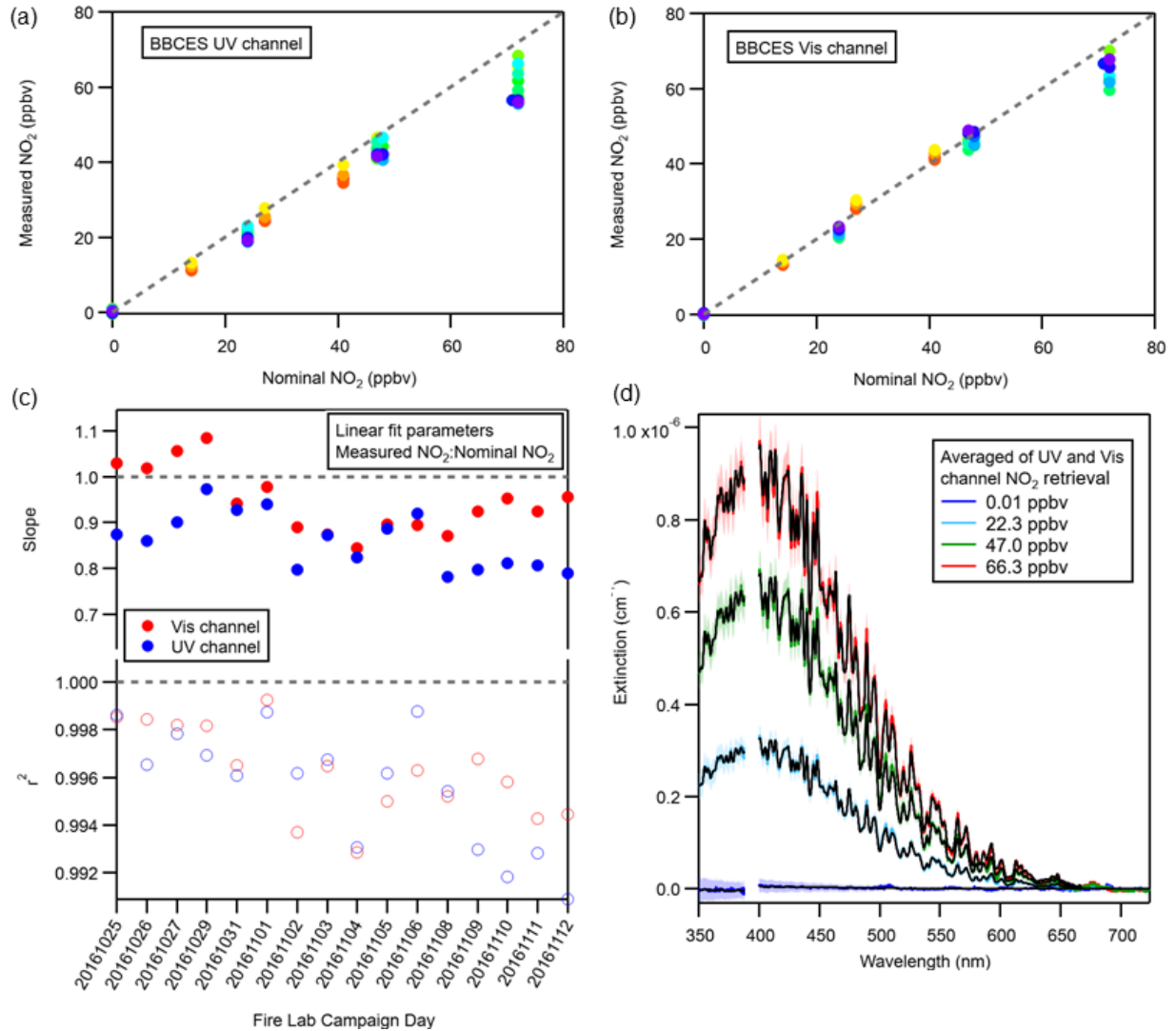
Figure S4. A demonstration of the SMPS correction described in Sect. 4.4. (a) Size distribution calculated from the SMPS inversion. It peaks at approximately 40 nm, and decreases towards larger diameters, as would be expected for an aerosol generated from an atomizer. However, above 750 nm, the distribution begins to exhibit structure that is not physically reasonable. The blue trace shows the same distribution, but with an upper threshold of 750 nm set, and any diameters than 850 nm are removed. (b) Inversions of the measured SMPS signal and with the elimination of particle diameters greater than 850 nm. (c) Size distributions for two diameter set points (225 and 450 nm) are shown, with the LAS in solid line, and SMPS in dashed line. While the two match reasonably well at lower diameters, there is a significant discrepancy above 850 nm. Because larger particles cause more light extinction, these spurious large peaks would contribute most of the light extinction, and therefore must be removed prior to RI retrieval.
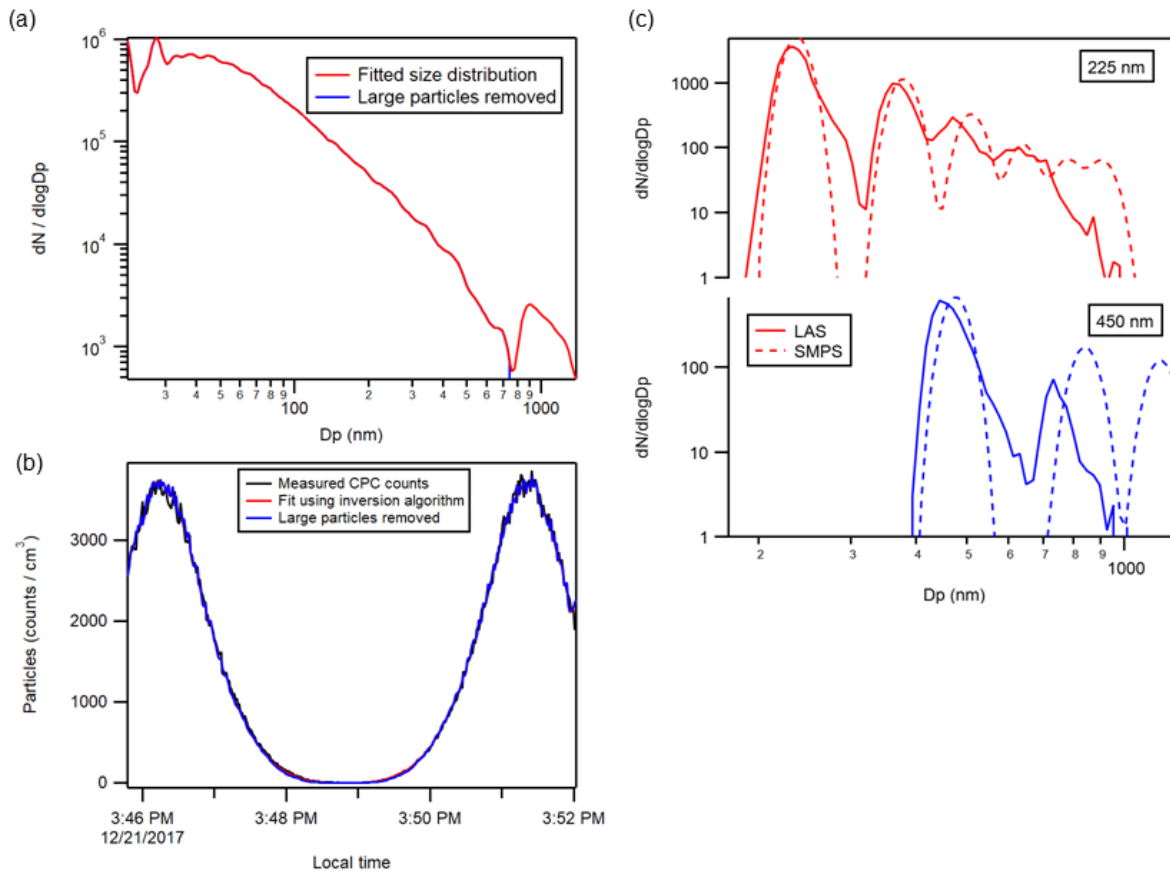
Figure S5. Theoretical calculation of the light scatter collected by the OPC optics as a function of diameter for several RIs. The black trace shows the expected scatter from PSL particles (1.59 + 0i) within the OPC solid angle collection optics angle of 14.8 and 57° from the perpendicular axis. This scatter is monotonically increasing in the relevant range of diameters for this work, and therefore the OPC is an accurate sizer of these particles. The red and blue traces show calculated scatter for particles with RIs of 1.65 + 0i and 1.65 + 0.1i respectively. The red trace begins to be non-monotonically increasing at lower diameters than the black trace, so would therefore be unable to effectively differentiate particles of diameter 675 - 700 nm and 800 - 850 nm. The blue trace shows the expected side-scattered light by moderately absorbing particles, and for these particles, the OPC would be unable to differentiate particles over 500 nm. This effect becomes increasingly pronounced at higher absorption RIs. This demonstrates the difficulty in sizing highly absorbing particles with an OPC.
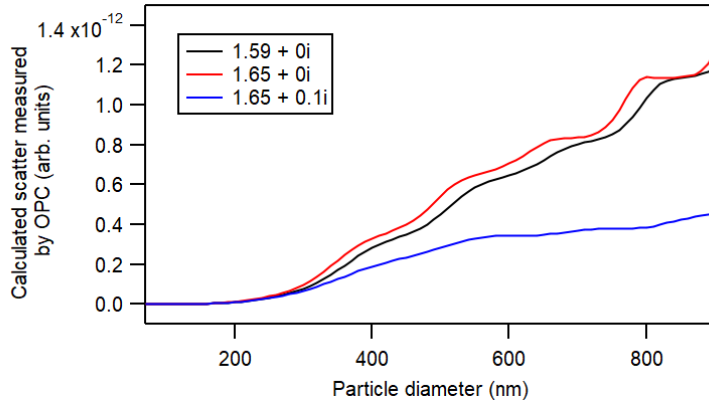
References

Danckaert, T., Fayt, C., Van Roozendael, M., De Smedt, I., Letocart, V., Merlaud, A., and Pinardi, G.: QDOAS Software user manual, Belgian Institute for Space Aeronomy, 2013.

Kraus, S. G.: DOASIS: A framework for DOAS, University of Mannheim, Mannheim, Germany, 2006.

Washenfelder, R. A., Langford, A. O., Fuchs, H., and Brown, S. S.: Measurement of glyoxal using an incoherent broadband cavity enhanced absorption spectrometer, Atmos. Chem. Phys., 8, 7779-7793, https://doi.org/10.5194/acp-8-7779-2008, 2008.